Astronomy & Astrophysics

Limb-darkening measurements for a cool red giant in microlensing event OGLE 2004-BLG-482[*]

M. Zub[1,2,3,4], A. Cassan[5,1,4], D. Heyrovský[6], P. Fouqué[7,4], H. C. Stempels[8], M. D. Albrow[9,4], J.-P. Beaulieu[5,4],
S. Brillant[10,4], G. W. Christie[11,12], N. Kains[13,4], S. Kozłowski[14,12], D. Kubas[5,10,4], J. Wambsganss[1,4], V. Batista[5],
D. P. Bennett[15], K. Cook[16], C. Coutures[5], S. Dieters[5], M. Dominik[13,**], D. Dominis Prester[17], J. Donatowicz[18],
J. Greenhill[19], K. Horne[13], U. G. Jørgensen[20], S. R. Kane[21], J.-B. Marquette[5], R. Martin[22], J. Menzies[23],
K. R. Pollard[9], K. C. Sahu[24], C. Vinter[20], A. Williams[22]
(The PLANET Collaboration)
A. Gould[14], D. L. DePoy[14], A. Gal-Yam[25], B. S. Gaudi[14], C. Han[26], Y. Lipkin[27], D. Maoz[28], E. O. Ofek[29],
B.-G. Park[30], R. W. Pogge[14], J. McCormick[31],
(The μFUN Collaboration)
A. Udalski[32], M. K. Szymański[32], M. Kubiak[32], G. Pietrzyński[32,33], I. Soszyński[32],
O. Szewczyk[32], and Ł. Wyrzykowski[32,34]
(The OGLE Collaboration)

(Affiliations can be found after the references)

ABSTRACT

Aims. We present a detailed analysis of OGLE 2004-BLG-482, a relatively high-magnification single-lens microlensing event that exhibits clear extended-source effects. These events are relatively rare, but they potentially contain unique information on the stellar atmosphere properties of their source star, as shown in this study.

Methods. Our dense photometric coverage of the overall light curve and a proper microlensing modelling allow us to derive measurements of the OGLE 2004-BLG-482source star's linear limb-darkening coefficients in three bands, including standard Johnson-Cousins I and R, as well as in a broad clear filter. In particular, we discuss in detail the problems of multi-band and multi-site modelling on the expected precision of our results. We also obtained high-resolution UVES spectra as part of a ToO programme at ESO VLT, from which we derive the source star's precise fundamental parameters.

Results. From the high-resolution UVES spectra, we find that OGLE 2004-BLG-482's source star is a red giant of MK type a bit later than M3, with $T_{\rm eff} = 3667 \pm 150$ K, $\log g = 2.1 \pm 1.0$ and an assumed solar metallicity. This is confirmed by an OGLE calibrated colour−magnitude diagram. We then obtain from a detailed microlensing modelling of the light curve linear limb-darkening coefficients that we compare to model-atmosphere predictions available in the literature, and find a very good agreement for the I and R bands. In addition, we perform a similar analysis using an alternative description of limb darkening based on a principal component analysis of ATLAS limb-darkening profiles, and also find a very good agreement between measurements and model predictions.

Key words. gravitational lensing: micro – stars: atmospheres – techniques: high angular resolution – stars: individual: OGLE 2004-BLG-482

1. Introduction

Photometric and spectroscopic observations of stars yield their spectral types and other information useful for studying their atmospheres, but much of the information on the structure of the atmosphere and related physical processes is lost in the disc-integrated flux. Advanced models calculated for a broad range of stellar types (e.g. MARCS, Gustafsson et al. 2008; ATLAS, Kurucz 1992; Plez et al. 1992) describe the corresponding physics at different optical depth, which can potentially result in observational signatures if the star's disc is spatially resolved. In particular, this information is present in the star's limb-darkening profile, which is the variation of intensity from the disc centre to the limb. Only a few observational

methods such as stellar interferometry, analyses of eclipsing binaries, transiting extrasolar planets and gravitational microlensing are able to constrain stellar limb-darkening in suitable cases. Every single measurement thus provides an important opportunity for testing stellar atmosphere models.

A Galactic gravitational microlensing event (Paczyński 1986) occurs when a foreground massive object passes in the vicinity of the line-of-sight to a background star, resulting in a transient brightening of the source star (called magnification, or amplification). Microlenses can spatially resolve a source star thanks to caustic structures created by a lens. They are formed by a single point or by a set of closed curves, along which the point-source magnification is formally infinite, with a steep increase in magnification in their vicinity. In practice, this increase is so steep that the characteristic length scale of the differential magnification effect is of the order of a fraction of the

---

source star's radius. Early works by e.g. Witt (1995) or Loeb & Sasselov (1995) have pointed out the sensitivity of microlensing light curves to limb-darkening, with the aim to help remove microlensing model degeneracies. The specific use of microlensing as a tool to study stellar atmosphere was proposed later (e.g. Valls-Gabaud 1995; Sasselov 1996; Hendry et al. 1998; Gaudi & Gould 1999), in particular to probe Galactic bulge red giant atmospheres (Heyrovský et al. 2000). Indeed, for a given microlensing configuration, the spatial resolution increases with the source's physical diameter, so that giant stars are primary targets.

Limb darkening measurements by microlensing were performed for a number of main-sequence and giant microlensed stars. Event MACHO 1998-SMC-1 (Albrow et al. 1999b; Afonso et al. 2000) allowed for the first time such a measurement for a metal-poor A6 dwarf located in the Small Magellanic Cloud (SMC). Its stellar type was derived from a spectroscopic and photometric analysis in five filters; the lens was a binary star also located in the SMC. No real comparison with atmosphere models could be provided since very little data existed for these metal-poor A stars. The first microlensing limb-darkening measurement for a solar-like star was reported by Abe et al. (2003): the source was identified as an F8-G2 main-sequence turn-off star, involved in the very high-magnification microlensing event MOA 2002-BLG-33 caused by a binary microlens. A good agreement with limb-darkening coefficient predictions was obtained in the I band. A limb-darkening measurement for the late G / early K sub-giant was also performed by Albrow et al. (2001) with the binary-lens caustic-crossing event OGLE 1999-BLG-23. The stellar type of the source star was identified by comparing its position on two colour−magnitude diagrams obtained from two different telescopes, and deriving the star's effective temperature from colour calibration. Again, they found a good agreement with stellar models both for the I and R filters.

Most of the limb-darkening measurements, however, were obtained on Galactic-bulge giant stars. The first case was reported by Alcock et al. (1997) for MACHO 95-30, which involved a very late M4 red giant source star (spectroscopic typing). In this event theoretical limb-darkening coefficients were only used to improve the light-curve fit, but no limb-darkening measurement has been performed. Heyrovský (2003) later argued that the intrinsic variability of the source star precluded any useful limb-darkening analysis. Late M giants are of special interest because they give access to testing models at the lower end of the temperature range used to compute most of the synthetic model atmosphere grids. For the event MACHO 1997-BLG-28, Albrow et al. (1999c) derived I and V coefficients for a K2 giant (typing from spectroscopic observations) crossing a caustic cusp, and found a good agreement with stellar models predictions. However, in such a complex event, many side effects could have affected the light curve, which somehow decrease the strength of the conclusions. Such a remark holds as well for MACHO 1997-BLG-41 (Albrow et al. 2000), which involved a late G5-8 giant crossing two disjoint caustics.

Microlensing event EROS BLG-2000-5 provided the first very good opportunity to test at high precision the limb-darkening of a K3 giant (typing based on both photometry and high-resolution spectroscopy) in five filters (Fields et al. 2003). They concluded that their results in the V, I, and H filters were discrepant from atmosphere models, and furthermore argued that the discrepancy is unlikely to be due to microlensing light-curve modelling drawbacks, but could rather be explained by inadequate physics in the stellar models that may be not applicable for all surface gravities. A clear variation with time in the

shape and equivalent width of the Hα line was also reported for the first time in this event (Afonso et al. 2001; Castro et al. 2001). Limb-darkening was also detected in OGLE 2003-BLG-238 (Jiang et al. 2004) and OGLE 2004-BLG-262 (Yoo et al. 2004), which involved early K1-2 giants, but no strong conclusions on limb darkening could be drawn from these events.

From the binary-lens event OGLE 2002-BLG-069 (Cassan et al. 2004; Kubas et al. 2005), it was possible to obtain not only limb-darkening measurements for a G5 bulge giant source star in the I and R bands, but also to directly test predictions from PHOENIX stellar model atmospheres by comparing the change of the Hα equivalent width during a caustic crossing (Cassan et al. 2004; Thurl et al. 2006) using high-resolution UVES/VLT spectra. A discrepancy was found between model and observations, which is most probably explained by the lack of a proper chromosphere implementation in the used stellar models. More recently, Cassan et al. (2006) performed limb-darkening measurements for the K3 giant source of OGLE 2004-BLG-254, and furthermore discussed an apparent systematic discrepancy between stellar model predictions and measurements that is observed for G-K bulge giants. However, in the case of OGLE 2004-BLG-254, it appeared that fitting all data sets together or only a subset of them had an influence on the limb-darkening measurements (Heyrovský 2008), which remove the observed discrepancy. In order to quantify this effect, we provide in this paper a detailed study on the impact of including data sets on the resulting limb-darkening measurements.

We model and analyse OGLE 2004-BLG-482, a relatively high-magnification single-lens microlensing event that exhibits clear extended-source effects. The source-star fundamental parameters and spectral typing were derived from a high-resolution spectrum obtained on VLT/UVES as part of a ToO programme. A good multi-site and multi-band coverage of the light curve allows us to extract linear limb-darkening coefficients, which we compare to model-atmosphere predictions.

The paper is organised as follows: in Sect. 2 we present the OGLE 2004-BLG-482 event, our photometric data and our data reduction procedures. We perform a detailed modelling of the light curve in Sect. 3. The fundamental properties of the target source star are derived in Sect. 4. Section 5 is dedicated to a detailed analysis of the measured linear limb-darkening coefficients and their comparison with model-atmosphere predictions. Finally in Sect. 6 we perform a similar analysis using an alternative description of limb-darkening based on a principal component analysis of a set of ATLAS limb-darkening profiles.

2. Photometric data

2.1. Event alert and follow-up observations

The Galactic microlensing event OGLE 2004-BLG-482 ($\alpha = 17^{\mathrm{h}}57^{\mathrm{m}}30.6^{\mathrm{s}}$, $\delta = -30°51'30''.1$ (J2000.0), or $l = -0.3392°$, $b = -3.1968°$) was discovered and publicly alerted on August 8, 2004 (MHJD[1] $\simeq 3226$) by the OGLE-III[2] Early Warning System ("EWS", Udalski 2003) on the basis of observations carried out in the I band with the 1.3 m Warsaw Telescope at Las Campanas Observatory (Chile).

Following this alert, the PLANET collaboration (*Probing Lensing ANomalies NETwork*) started its photometric follow-up observations on August 10, 2004 (MHJD $\simeq 3228$), using a network of ground-based telescopes, including the Danish

---

[1] Modified Heliocentric Julian Date: MHJD = HJD − 2 450 000

[2] http://ogle.astrouw.edu.pl
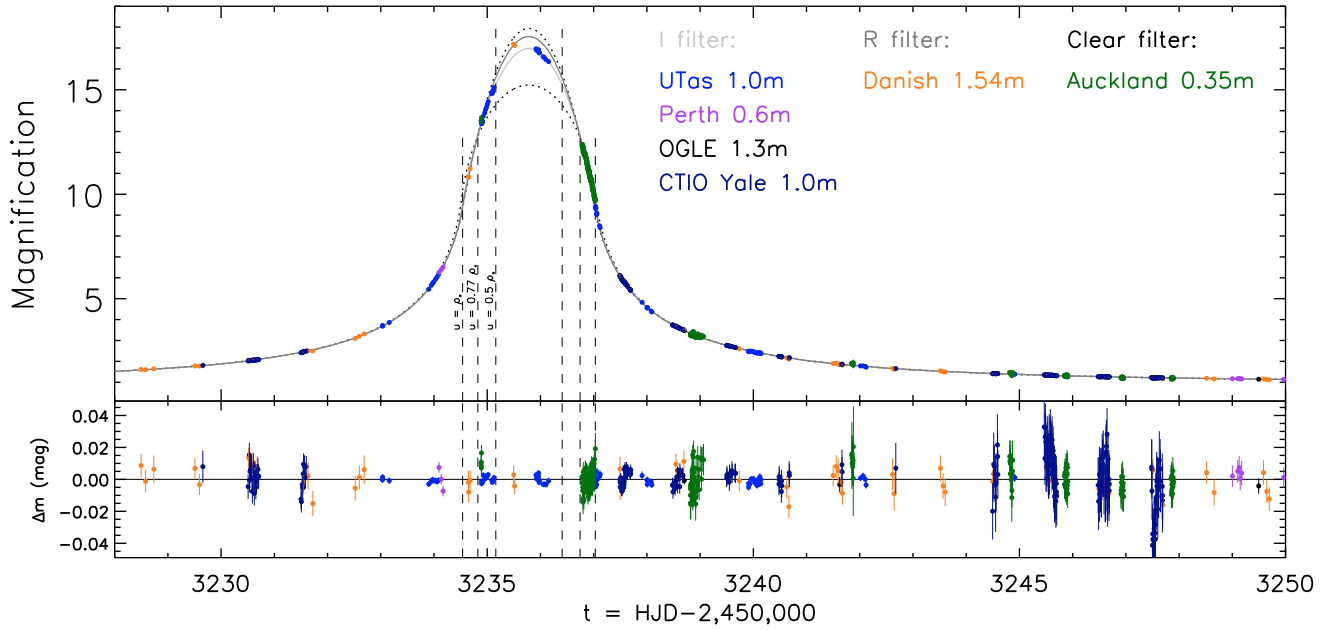
Fig. 1. Light curve of OGLE 2004-BLG-482, with data from PLANET (Danish, UTas and Perth), OGLE and μFUN (CTIO-Yale and Auckland) collaborations. The two gray solid lines in the upper panel draw the best-fit model for the I and R filters with linear limb-darkening parameters given in Table 2. The two dotted curves correspond to the two extreme cases, $\Gamma = 0$ (uniformly bright source, lower dotted curve) and $\Gamma = 1$ (upper dotted curve). The two pairs of vertical dashed lines marked $u = \rho_*$ and $u = 0.5\,\rho_*$ indicate when the lens is located at the limb of the source and half way from its centre to the limb. All the curves intersect at $u = 0.77\,\rho_*$, also marked by a vertical dashed line. The fit residuals in magnitudes are displayed in the lower panel.

1.54 m (La Silla, Chile), Canopus 1 m (Hobart, Tasmania), and Perth/Lowell 0.6 m (Bickley, Western Australia) telescopes. Data sets and quasi real-time fitted light curves were made publicly available online[3], as part of a general data sharing policy. The event was also monitored by the μFUN collaboration[4], which gathered data from six telescopes: the 1.3 m and Yale 1.0 m (Cerro Tololo Inter-American Observatory, Chile), the Palomar 1.5 m telescope (Palomar Observatory, USA), Wise 1 m (Mitzpe Ramon, Israel), and two New Zealand amateur telescopes at Auckland (0.35 m) and Farm Cove (0.25 m).

On August 15, 2004 (MHJD $\simeq$ 3233), photometric data indicated a deviation from a normal point-source point-lens light curve. A public alert was issued on August 16, 2004 16:05 UT, pointing towards a high peak magnification event, possibly featuring strong extended-source size effects. In the following hours, on August 17, 2004 a target of opportunity (ToO) was activated on the UVES spectrograph at ESO VLT in order to monitor the event peak magnification region where spectroscopic effects are expected. Thanks to an almost real-time modelling operated in parallel, the crossing time of the source disc by the lens was estimated to be around 2.4 days. The peak of the light curve was reached on August 18, 2004 18:32 UT at almost three magnitudes above the baseline, corresponding to a minimum (i.e. with null blending) peak magnification of $A \sim 15$.

2.2. Data reduction and error bars

The OGLE data were reduced with their own pipeline, while PLANET and μFUN data were reduced with various versions of the PLANET pipeline (pySIS; Albrow et al. 2009). All these reductions are based on the image-subtraction method

---

[3] http://planet.iap.fr
[4] http://www.astronomy.ohio-state.edu/~microfun

Table 1. Final selection of data sets, with the raw number of observational data (frames) and our final selection after the cleaning process.

Telescope	Filter	Data	(Frames)	k_σ
UTas (PLANET)	I	86	(128)	2.4
Perth (PLANET)	I	13	(15)	3.8
OGLE	I	44	(68)	2.4
CTIO-Yale (μFUN)	I	233	(285)	4.2
Danish (PLANET)	R	51	(67)	3.2
Auckland (μFUN)	(clear)	266	(334)	2.4
All data	–	693	(897)	–

Notes. The last column lists the adopted error-bar rescaling factors.

(Alard & Lupton 1998; Bramich 2008). A preliminary image-quality inspection helped to remove images with a significant gradient across the field, owing to strong background moonlight. Under-exposed images were also removed in this process. We paid particular attention to the quality of data taken at La Silla at the time of peak magnification, because of unfavourable weather conditions at that site. We could however keep a few trusted data points.

After the data reduction process, we set for each PLANET and μFUN telescope a range of seeing and background within which the homogeneity of the data sets is ensured. For the Yale telescope, we excluded data with seeing outside the range 1.8−3.2″. In the case of UTas data, we applied an upper limit on the seeing of 3.0″, and for the Perth, Danish, and Auckland telescopes, 3.3″. Our final data set is presented in Table 1 and displayed in Fig. 1 (Auckland telescope had no filter at the time of the observation, so the filter is referred to as *clear*).

It is known that the error bars we obtain from the data reduction are usually underestimated, and are not homogeneous from one data set to another. To avoid this problem, we rescaled

the error bars, so that from the best model one has $\chi^2/N \simeq 1$ for each data set fitted alone, with N the corresponding number of data points. Moreover, it happens that some of the original error bars σ are unrealistically small; to prevent this, we added in quadrature an additional term to the rescaled error bars, so that $\sigma'^2 = (k_\sigma \sigma)^2 + (4 \times 10^{-4})^2$ magnitudes. When the original error bars are small (UTas and Danish), the constant term dominates the error bars' size. The values of k_σ are given in Table 1.

3. Light-curve modelling

3.1. Linear limb-darkening formalism

Limb-darkening profiles of stars can be described analytically at different levels of approximation, in particular by a sum containing powers of $\mu = \cos\alpha$, where α is the angle of a given emerging light ray with respect to the normal of the stellar surface (e.g. Claret 2000). In the first degree of approximation, called the *linear limb-darkening* (hereafter, LLD) law, the star brightness profile can be written as

$$I(r) = 1 - a\left(1 - \sqrt{1 - r^2}\right), \tag{1}$$

where $r = \sqrt{1 - \mu^2}$ is the fractional radius on the stellar disc from where the light is emitted, and a is the *linear limb-darkening coefficient* (hereafter LLDC). In this work, we will concentrate on measuring LLDCs. Firstly, because in microlensing events higher order coefficients have a very small impact, e.g. Dominik (2004) finds that for a caustic crossing, the effect of the change of the LLDC on light curve is $\sim$25 times greater than the square-root coefficient. Secondly, because a strong correlation exists between the coefficients, it is impossible to precisely measure the LLDC when a further coefficient is taken into account (Kubas et al. 2005). Lastly, because LLDC are widely used and are available in catalogues; it is an important aspect for our goal to compare our results with the existing literature.

For our modelling purpose, a more convenient way to rewrite the LLD law is to have a formula that conserves the total source flux for all LLDC values. With this requirement, the LLD law equivalent to Eq. (1) (Albrow et al. 1999a) but normalised to unit flux can be written as

$$I(r) = \frac{1}{\pi}\left[1 - \Gamma\left(1 - \frac{3}{2}\sqrt{1 - r^2}\right)\right], \tag{2}$$

where Γ is the LLDC modelling parameter, with

$$a = \frac{3\,\Gamma}{2 + \Gamma}. \tag{3}$$

With this formalism, it is interesting to notice that all limb-darkening profiles intersect at a common fractional radius (Heyrovský 2003), $r_{\mathrm{lld}} = \sqrt{5}/3 \simeq 0.75$.

3.2. Single-lens, extended-source models

In its motion relative to the lens, the source centre approaches the lens at a minimal distance u_0 in units of the angular Einstein ring radius $\theta_{\mathrm{E}} = \sqrt{4GMc^{-2}\left(D_{\mathrm{L}}^{-1} - D_{\mathrm{S}}^{-1}\right)}$ (Einstein 1936, with D_{S}, D_{L} the distances from the source and the lens to the observer, M the lens mass), which can be smaller than the source radius ρ_* expressed in the same units. Because high-magnification events involve low values of the impact parameter u_0, they are likely to

be affected by extended-source effects in particular if the source star is a giant. Although this happens fairly rarely in practice (a couple of cases amongst the $\sim$700 microlensing events observed every year), this is the case for OGLE 2004-BLG-482.

The point-source magnification at the exact location of the lens is formally infinite, following the well-known formula (Paczyński 1986)

$$A_{\mathrm{pspl}}(u) = \frac{u^2 + 2}{u\sqrt{u^2 + 4}}, \tag{4}$$

where u is the distance from the lens to a given point on the source in units of θ_{E}. Consequently, the flux originating from regions of the source in the immediate neighbourhood of the lens (typically a fraction of the source radius) is preferentially amplified. The relative motion of the source and lens then results in a time-dependent probing of the stellar atmosphere at different fractional radius, corresponding to different optical depths.

Single-lens light curves affected by extended-source effects display a characteristic flattening at their peak. For a uniformly bright extended source, Witt & Mao (1994) derived an exact analytic formula for the magnification, which involves elliptic integrals. But there is no similar formula to describe limb-darkened sources, and calculating the exact magnification requires numerical integration. One way is to decompose the source into small rings of uniform intensity. Another approach by Heyrovský (2003) is to perform the angular integration over the stellar disc analytically and only the radial integration numerically, for arbitrary sources.

If some conditions are fulfilled, it is also possible to use approximate formulae, which have the advantage to allow us a very fast computation. Considering that in Eq. (4), $A_{\mathrm{pspl}} \simeq 1/u$ when $u \ll 1$, Yoo et al. (2004) find that the magnification A_{lld} for an extended source with a linear limb-darkening profile with coefficient Γ can be expressed as

$$\begin{aligned}
A_{\mathrm{lld}}(u, \rho_*) &= [B_0(z) - \Gamma B_1(z)] A_{\mathrm{pspl}}(u), \\
z &= u/\rho_*, \\
B_0(z) &= \frac{4\,z}{\pi} E\left[\arcsin\min\left(1, \frac{1}{z}\right), z\right], \\
B_1(z) &= B_0(z) - \frac{3\,z}{\pi}\int_0^\pi\int_0^1 \frac{r\sqrt{1 - r^2}}{\sqrt{r^2 + z^2 - 2\,z\,r\cos\phi}}\,\mathrm{d}r\,\mathrm{d}\phi,
\end{aligned} \tag{5}$$

where E is the incomplete elliptic integral of the second kind following the notation of Gradshteyn & Ryzhik (1965). The integral B_1 can be efficiently evaluated and tabulated for z, as can B_0. This approximation is valid as far as $\rho_*^2/8 \ll 1$ and $u_0 \ll 1$. Because these relations hold for OGLE 2004-BLG-482 we choose this formalism (although close to the limit case of application, since the maximum error for a uniform source here is of the order of 0.2%, but is still much lower than the photometric errors).

The complete model then involves four parameters: the source radius ρ_*, as well as u_0, t_0 and t_{E}, which define the rectilinear motion of the source with respect to the lens, so that the lens-source separation u satisfies $u^2(t) = u_0^2 + (t - t_0)^2/t_{\mathrm{E}}^2$. Moreover, one has to take into account for each telescope "i" two more parameters, the baseline magnitude $M_{\mathrm{b}}^i = -2.5\log(F_{\mathrm{S}}^i + F_{\mathrm{B}}^i)$ and the blending factor $g^i = F_{\mathrm{B}}^i/F_{\mathrm{S}}^i$. Here, F_{S}^i and F_{B}^i are the source and the blend flux, the latter referring to any un-magnified flux entering the photometric aperture, from the lens itself and e.g. background stars. They are related to the time-dependent magnification A_{lld} by $F^i(t) = A_{\mathrm{lld}}(t)F_{\mathrm{S}}^i + F_{\mathrm{B}}^i$.

3.3. Fitting procedure

To fit our data sets, we use two minimisation schemes: Powell's method and a Markov-Chain Monte-Carlo algorithm, from which we also obtain the model parameter error bars (Kains et al. 2009; Cassan et al. 2010). As stated before, it is impossible to define a proper number of degrees of freedom. Indeed, the parameters u_0, t_0, t_E and ρ_* are common to all data sets, whereas M_b^i and g^i are associated to the data set "i", and the LLDCs may be chosen to be common per observing filter or per individual telescope. This explains the choice of N instead of d.o.f. to rescale the error bars in Sect. 2.2. The first requirement to get precise measurements of limb-darkening coefficients is to get an overall well-covered light curve. This allows us to secure good measurements of the basic parameters u_0, t_0, t_E and ρ_*, as well as M_b^i and g^i. The region of the light curve with a noteworthy sensitivity to limb-darkening is, however, mainly limited to when the lens is inside the source-star disc, and drops to a few percent outside (Heyrovský et al. 2000). We now discuss this aspect in greater detail.

While all limb-darkening profiles intersect at the same fractional radius $r_{lld} \simeq 0.75$ as seen in Sect. 3.1, the corresponding magnification light curves intersect at around $u_{lld} \simeq 0.77\,\rho_*$ (with u the lens-source centre distance). This special point is marked by a vertical dashed line in Fig. 1, in which we have also indicated two other interesting positions of the lens: at the limb of the source ($u = \rho_*$) and at half-way from its centre to its limb ($u = 0.5\,\rho_*$). The two dotted magnification curves of the figure show the two extreme cases of LLDC, $\Gamma = 0$ (no limb-darkening) and $\Gamma = 1$. From this we can distinguish three main regions: $0 < u/\rho_* < 0.5$, where the limb-darkening sensitivity is high, up to ~16%; $0.5 < u/\rho_* < 0.77$, where the sensitivity decreases outward to 0, and $0.77 < u/\rho_* < 1$ where the sensitivity increases outward and peaks at the limb at ~8% (Heyrovský 2003). Based on this argument and from our data coverage of OGLE 2004-BLG-482 shown in Fig. 1, it is clear that we can expect LLDC measurements from UTas I-band, Danish R-band and Auckland's clear-filter.

The best-fit parameters and their error bars are given in Table 2 for different combinations of data sets. We comment on the results in detail in Sects. 5 and 6. In Fig. 1 we plot the combined fit including all telescopes and using one coefficient per band.

3.4. Estimates of the lens properties

Although the properties of the lens are not of primary interest here, we can still provide an estimate of the lens' mass and distance. However, these quantities cannot be measured here, because an additional observable, such as the parallax, is needed to remove a degeneracy between these two parameters. Here, parallax effects are not visible because the time scale of the event is very short, $t_E \simeq 10$ days $\ll 1$ year.

From our modelling and our estimate of the source radius and distance (see Sect. 4.1), we derive the Einstein radius to be around $\theta_E = \theta_*/\rho_* \simeq 0.4$ mas, which leads to a relative proper motion of $\mu = \theta_E/t_E \simeq 16$ mas/yr. This high proper motion almost certainly means that the lens is located in the disc (or possibly in the halo). Moreover, with such a high motion, there is a good chance that the lens can be clearly visible (away from the source) in a few years by adaptive optics observations.
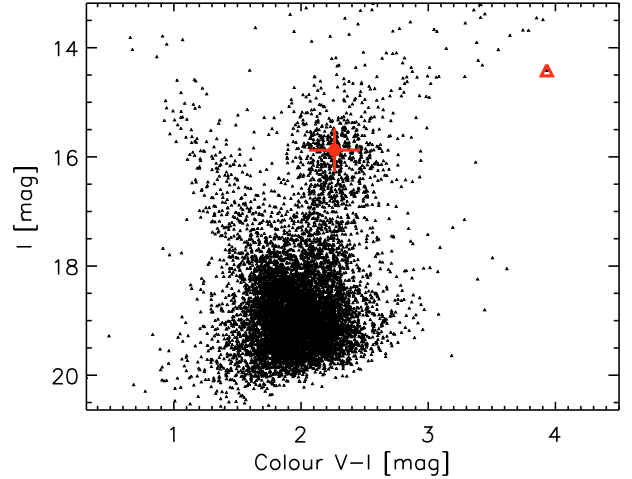
Fig. 2. OGLE-III BLG182.8 field calibrated I vs. $(V - I)$ colour–magnitude diagram, comprising stars within a radius of 2.16′ centred on our target OGLE 2004–BLG–482 (red open triangle). The red circle indicates the mean position of the RCG centre, and the cross the width of the two-dimensional Gaussian distribution.

4. Source star properties

4.1. OGLE calibrated colour–magnitude diagram

The microlensing event OGLE 2004-BLG-482 occurred in OGLE-III BLG182.8 field, and was also observed during the second phase of OGLE in field BUL_SC23. From the calibrated photometry in I and V filters of the OGLE-III BLG182.8 field, we extract an I vs. $(V - I)$ colour−magnitude diagram (CMD) by selecting stars surrounding our target within a circle of radius 2.16′ (~9000 stars), as shown in Fig. 2. This choice ensures that we have enough stars to construct the CMD while keeping a reasonably homogeneous extinction across the selected region.

Our target is indicated as the red open triangle and has a calibrated magnitude and colour of $I = 14.41 \pm 0.03$ and $(V - I) = 3.93 \pm 0.04$. From the analysis of the OGLE images, we conclude that this bright target is not blended by a neighbouring star in I. We also checked in the OGLE-III photometric catalogue, which has a better resolution than OGLE-II, that there is no blended star within 1 arcsec bright enough in V to contaminate our measurements. Finally, our model finds a blending ratio close to zero, justifying our assumption that the measured magnitude and colour of the target can safely be assigned to the source star.

In order to correct these measurements for extinction, we can either use the reddening maps of Sumi (2004) based on OGLE-II photometry, or use the red clump giant (RCG hereafter) assuming that our source suffers the same amount of extinction. At the position of the source, Sumi (2004) measures an extinction of $E(V - I) = 1.405 \pm 0.027$. This is derived assuming a clump colour of 1.028 and a ratio of total to selective extinction $R_I = 0.964$, giving an absorption of $A_I = R_I \times E(V - I) = 1.36 \pm 0.06$.

The RCG central position is marked in Fig. 2 as a red circle with error bars. To determine its mean magnitude and colour, we fit a two-dimensional Gaussian around its position (~400 stars), from which we derive $I_{RCG} = 15.88 \pm 0.01$ and $(V - I)_{RCG} = 2.263 \pm 0.004$. Using the same clump colour as Sumi (2004), we get an extinction of $E(V - I) = 1.235$. Given the uncertainty of the intrinsic clump colour, due to variations with age and metallicity (Salaris & Girardi 2002), this estimate agrees with the previous one. We therefore adopt as the dereddened magnitudes and

colour of our target $I_0 = 13.05 \pm 0.07$, $(V - I)_0 = 2.53 \pm 0.05$ and $V_0 = 15.58 \pm 0.09$.

In principle the observed position of the clump could be used to measure its distance. In practice, the absolute magnitude of the clump depends on age and metallicity, and corrections introduce an uncertainty as for its intrinsic colour. Moreover, the reddening corrections are not accurately determined. We therefore prefer fixing the distance and check that the observed clump position is compatible with this choice. We start by assuming a Galactic Centre distance of 8.33 ± 0.35 kpc from Gillessen et al. (2009), giving a distance modulus of 14.60 ± 0.09. Then, we assume that Baade's Window at ($l = 1.00°$ $b = -3.88°$) is at about the same distance as the Galactic Centre, according to Paczyński & Stanek (1998). This fixes the distance to OGLE-II field BUL_SC45, which contains Baade's Window. Finally, we use the relative distance of field BUL_SC23 with respect to BUL_SC45 as given by Rattenbury et al. (2007) (their Table 1), which amounts to 0.13 mag, to get a distance modulus of 14.73 ± 0.15 to the clump in the direction of our target. The corresponding absolute magnitude of the clump is then $15.88 - 1.36 - 14.73 = -0.21$, in good agreement with the most recent value determined by Groenewegen (2008) for the local red clump based on revised Hipparcos data, namely $M_{I,\mathrm{RCG}} = -0.22 \pm 0.03$.

If our source is at the same distance as the clump in its direction and suffers the same amount of extinction, its expected dereddened magnitude is $14.41 - 15.88 + 14.51 = 13.04$, in good agreement with the previous estimate based on Sumi's reddening law. The agreement in colour is not as good, at $3.93 - 2.263 + 1.028 = 2.70$.

We then fit calibrated isochrones from Bonatto et al. (2004) to 2MASS data in our field, to derive the following near-infrared extinctions: $A_J = 0.52 \pm 0.10$, $A_H = 0.36 \pm 0.11$ and $A_{K_s} = 0.20 \pm 0.02$. From this and the magnitudes listed in the 2MASS PSC for our target (2MASS 17573061-3051305), we get $J_0 = 11.55 \pm 0.10$, $H_0 = 10.68 \pm 0.11$ and $K_{s,0} = 10.42 \pm 0.04$, and the corresponding colours $(J - H)_0 = 0.87 \pm 0.16$, $(H - Ks)_0 = 0.26 \pm 0.12$ and $(J - Ks)_0 = 1.13 \pm 0.11$. Converting to Bessell & Brett near-infrared photometric system (Bessell & Brett 1988) gives $(J - Ks)_0 = 1.17$ and $K_0 = 10.46$, corresponding to an M4 giant (their Table 3), which have mean colours of $(V - I)_0 = 2.55$ and $(V - K)_0 = 5.10$, in good agreement with our observed values $(V - I)_0 = 2.53$ and $(V - K)_0 = 15.58 - 10.46 = 5.12$.

This allows us to estimate the source radius using the surface brightness relation: $\log \theta_* + K_0/5 = (0.037 \pm 0.007) \times (V - K)_0 + (0.610 \pm 0.028)$ from Groenewegen (2004) calibrated on 40 M giants, where θ_* is the source angular diameter in *mas*. We find an angular diameter of $\theta_* = 51 \pm 3$ μas, which at the adopted source distance of $d = 8.8 \pm 0.6$ kpc corresponds to a physical source radius of $R_* = 48 \pm 4$ $R_\odot$.

In the next section, we perform the analysis of the VLT/UVES high-resolution spectra that we obtained on this event, in order to derive more accurately the spectral type and to determine the fundamental parameters of the source star.

4.2. VLT/UVES spectroscopy

We have obtained for OGLE 2004-BLG-482 high-resolution spectra ($R \sim 40\,000$) on VLT/UVES, as part of a ToO activated shortly after the peak of the light curve was passed. The data were reduced in a standard way using version 2.1 of the UVES context of the MIDAS data reduction software.

The spectrum is dominated by broad absorption bands from molecules. The shape and depth of molecular absorption bands, particularly TiO, are very sensitive to the stellar effective

temperature T_{eff}, and to a lesser degree also to the surface gravity $\log g$. We estimated the atmospheric parameters of OGLE 2004-BLG-482 by comparing the observed spectrum with a grid of pre-calculated synthetic template spectra.

The grid of synthetic template spectra, calculated by Plez (priv. comm.), is based on synthetic spectra calculated from MARCS spherical model atmospheres with 1D emergent spectra and LTE radiative transfer (Gustafsson et al. 2008, 2003, 1975; Plez et al. 2003, 1992), and includes the latest available atomic and molecular line data (Gustafsson et al. 2008; Kupka et al. 1999; Plez 1998). Synthetic template spectra for M giants calculated with the MARCS model atmospheres have a good record for determining stellar parameters in M supergiants (e.g. Levesque et al. 2005, 2007; Massey et al. 2008) and were extensively used to calibrate M giant photometry (Bessell et al. 1998).

The grid used in our analysis covers an effective temperature range of 3000 K $< T_{\mathrm{eff}} <$ 4000 K, with steps of 100 K, and a surface gravity range of $0.0 < \log g < 3.0$, with steps of 0.5. This grid was calculated for giants with solar abundances and no carbon enrichment. Since our grid does not cover a range of metallicities, we therefore have no leverage on this parameter. We also prepared routines to calculate linear interpolations between the spectra in our grid for any given value of T_{eff} and $\log g$.

We then compared the observed spectrum of OGLE 2004-BLG-482 with template spectra across the available range of T_{eff} and $\log g$ and determined the goodness-of-fit using the χ^2 diagnostic. In calculating χ^2, we used the entire observed spectrum, from approximately 4800 to 10 000 Å, only excluding three regions that are strongly affected by telluric absorption (7580−7850, 9070−9120 Å and 9300−9800 Å). However, since no continuum is present in our spectrum, and we also do not know the absolute stellar flux, we renormalised the synthetic spectrum using a one-dimensional polynomial function prior to calculating χ^2. This renormalisation does not affect the shape of the broad molecular bands that are important for determining T_{eff} and $\log g$.

We refined the best values of T_{eff} and $\log g$ using parabolic minimisation between the grid points that yielded the lowest value of the χ^2 diagnostic. In Fig. 3 we illustrate the agreement between the observed and best-fit template spectrum, including estimated parameter uncertainties, around the highly temperature-sensitive TiO band near 7100 Å. We find that the parameters that best fit our observed spectrum are $T_{\mathrm{eff}} = 3667 \pm 150$ K and $\log g = 2.1 \pm 1.0$, assuming solar abundances. The quoted error bars are dominated by systematic uncertainties in the synthetic spectra and data reduction procedures used, such as flux calibration. Our uncertainties are further increased because our grid of template spectra was calculated for only one metallicity. The range of effective temperatures we find is compatible with a star of MK spectral type between M1 and M5, with the best-fit value giving a red giant star a bit later than M3 (Houdashelt et al. 2000; Strassmeier & Schordan 2000).

The large error bar on the surface gravity confirms that our spectrum has little to offer in gravity-sensitive diagnostics. However, we can obtain independent constraints on $\log g$: given that the mass of an M giant of 1 or 10 Gyr is smaller than 2.3 and 1 $M_\odot$ respectively, using $\log g = \log g_\odot + \log M - 2 \times \log R_*$, we find the corresponding upper limits of the surface gravity: $\log g = 1.5 \pm 0.2$ and $\log g = 1.1 \pm 0.2$ respectively, taking into account the uncertainty of the source radius. This agrees with our spectroscopic analysis, although favouring the lower boundary.
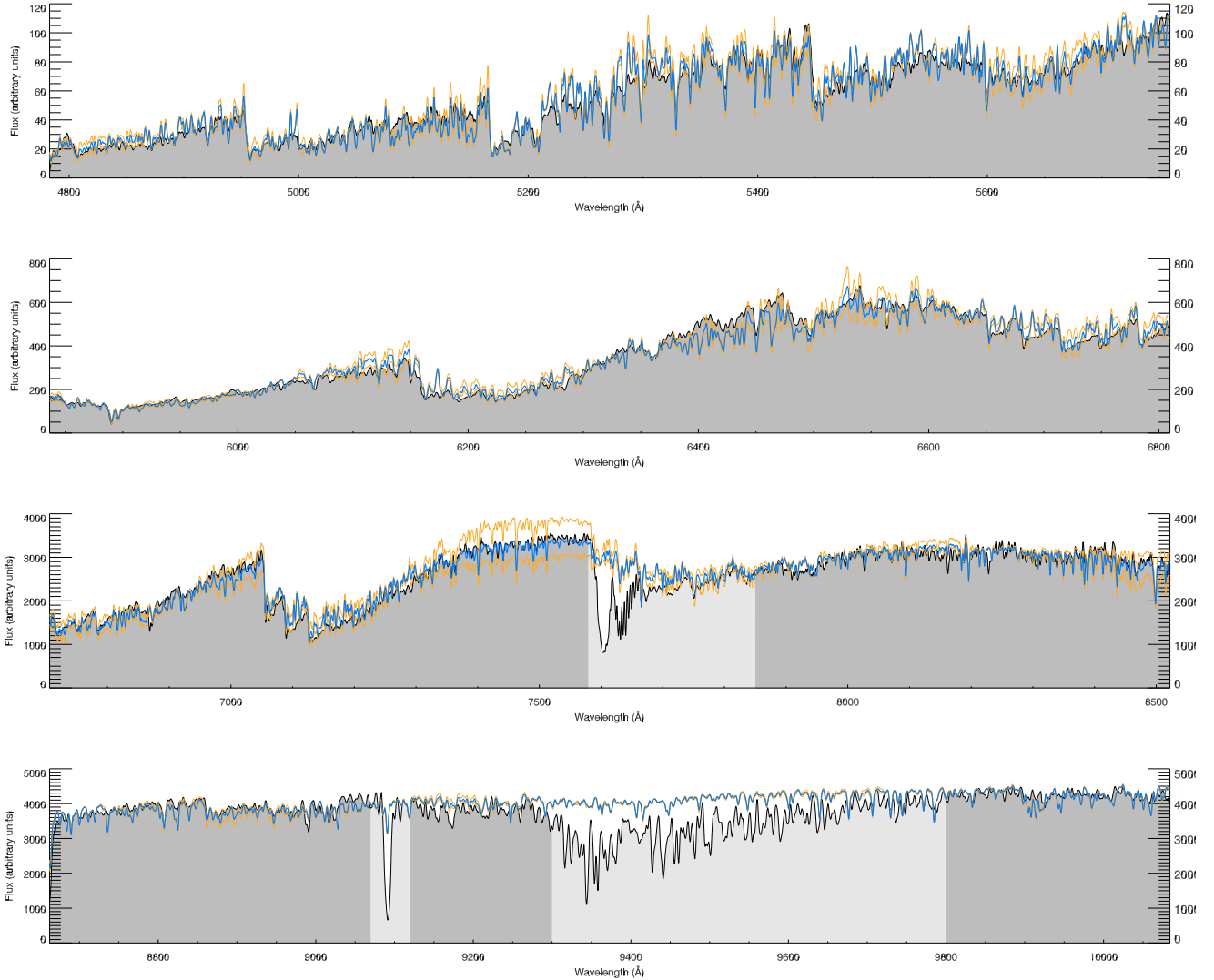
Fig. 3. Observed (black line) and best-fit (blue) template spectrum of OGLE 2004-BLG-482. The region around the TiO 7100 shows the agreement of the observed and synthetic spectra. The two orange curves are plotted at ±100 K. The regions excluded from the fitting process are shaded in light grey, while the remainder of the spectrum is shaded in dark grey.

4.3. Conclusion on the source MK type and parameters

We finally find a good agreement between our photometric and spectroscopic study, with a source star of MK spectral type a bit later than M3. We therefore adopt the fundamental parameters from the spectroscopic analysis ($T_{\rm eff}$ = 3667 ± 150 K, $\log g$ = 2.1 ± 1.0, solar metallicity) to make our selection of atmosphere models used to compare our limb-darkening measurements to model predictions, as discussed in the next section.

5. Linear limb-darkening discussion

As discussed in Sect. 3.3, three data sets have some sensitivity to limb-darkening: UTas (*I*-band), Danish (*R*-band) and Auckland (clear filter). The first question we address now is how the individual linear limb-darkening coefficients (LLDC) are affected by including or removing some of our data sets. Indeed, our first step was to model every data set independently, and step by step to include other telescopes. We first noticed that there was a change in the LLDC values that depends on the added data sets. We therefore performed a detailed analysis to understand what could cause such variations, and to identify combinations of data sets that lead to correct LLD measurements. The results

we are commenting are presented in Fig. 4: the three columns correspond to UTas, Danish, and Auckland, respectively, and the individual panels display the LLDC measurements for various combinations of data sets; the corresponding model parameters are given in Table 2. In the figure and table, the letters A, C, D, O, P, U refer to the telescopes Auckland, CTIO Yale, Danish, OGLE, Perth, and UTas respectively.

UTas (U) clearly provides the best data set for LLDC measurements, since the data sample the whole LLD-sensitive region at the peak of the light curve, as well as its wings and baseline. On the other hand, modelling Danish (D) alone provides a very unrealistic fit, with large error bars and very irregular MCMC correlations. To explain this, we recall that as mentioned in Sect. 2.2, the peak of the light curve was observed under bad weather conditions in La Silla, in particular the two consecutive data points around t = 3235.5. Moreover, the data coverage is not optimal, because there are only two epochs that cover the LLD-sensitive part of the light curve. As a result, this poor coverage combined with some uncertainty in the data lead to a model that apparently looks better in terms of chi-squared, but cannot be trusted. The last telescope with data sensitive to limb darkening is Auckland (A). We can fit the corresponding data alone and obtain a reasonable fit, but

Table 2. Model parameters and error bars for different relevant combinations of data sets.

| Parameters	UTAS (U)	DANISH (D)	AUCKLAND (A)	OGLE (O)	PERTH (P)	CTIO YALE (C)
	Independent fits for U, D and A					
t_0 (days)	3235.78(4 ± 1)	3235.78(3 ± 3)	3235.76(8 ± 4)	–	–	–
u_0	0.010(8 ± 4)	0.0(2 ± 1)	0.0(0 ± 1)	–	–	–
t_E (days)	8.(9 ± 1)	9.(6 ± 4)	9.(3 ± 3)	–	–	–
ρ_*	0.14(0 ± 2)	0.1(3 ± 1)	0.14(0 ± 7)	–	–	–
a	**0.677 ± 0.013**	**0.67 ± 0.22 [⋆]**	**0.76 ± 0.13**	–	–	–
M_b	11.5	11.4	13.5	–	–	–
g	7.0	1.4	4.5	–	–	–
χ^2	82.5	43.2	234.9	–	–	–
	Combined fit including U+D					
t_0 (days)	3235.784(5 ± 8)					
u_0	0.00(9 ± 2)					
t_E (days)	9.1(5 ± 9)					
ρ_*	0.13(7 ± 1)					
a	**0.674 ± 0.012**	**0.837 ± 0.018**	–	–	–	–
M_b	11.5	11.4	–	–	–	–
g	7.2	1.3	–	–	–	–
χ^2	85.1	57.8	–	–	–	–
	Combined fit including U+A					
t_0 (days)	3235.780(8 ± 8)					
u_0	0.00(0 ± 3)					
t_E (days)	9.(1 ± 1)					
ρ_*	0.13(8 ± 2)					
a	**0.714 ± 0.013**	–	**0.660 ± 0.023**	–	–	–
M_b	11.5	–	13.5	–	–	–
g	7.2	–	4.5	–	–	–
χ^2	101.9	–	286.3	–	–	–
	Combined fit including D+A					
t_0 (days)	3235.77(5 ± 3)					
u_0	0.00(0 ± 7)					
t_E (days)	9.(7 ± 2)					
ρ_*	0.13(4 ± 8)					
a	–	**1.0 ± 0.23 [⋆]**	**0.93 ± 0.29 [⋆]**	–	–	–
M_b	–	11.4	13.5	–	–	–
g	–	1.4	4.8	–	–	–
χ^2	–	50.6	241.5	–	–	–
	Combined fit including U+D+A					
t_0 (days)	3235.781(4 ± 9)					
u_0	0.00(0 ± 4)					
t_E (days)	9.2(9 ± 6)					
ρ_*	0.13(6 ± 1)					
a	**0.713 ± 0.012**	**0.881 ± 0.010**	**0.660 ± 0.011**	–	–	–
M_b	11.5	11.4	13.5	–	–	–
g	7.3	1.3	4.6	–	–	–
χ^2	102.7	58.1	287.8	–	–	–
	Combined fit including all telescopes (one LLDC per band)					
t_0 (days)	3235.781(6 ± 7)					
u_0	0.00(0 ± 2)					
t_E (days)	9.6(1 ± 2)					
ρ_*	0.130(9 ± 5)					
a	**0.714 ± 0.010**	**0.884 ± 0.021**	**0.652 ± 0.016**	**0.714 ± 0.010**	**0.714 ± 0.010**	**0.714 ± 0.010**
M_b	11.5	11.4	13.5	14.1	12.7	14.0
g	7.6	1.4	4.8	0.0	0.7	−0.8
χ^2	122.7	51.0	286.6	42.6	14.3	239.7

Notes. The measured linear limb-darkening coefficients are indicated in bold face. The data sets are referred to by letters, following the convention indicated in the first line of the table. The uncertainties on the parameters are indicated in parenthesis and apply to the last significant digit. Models for which no stable fit or very unrealistic results are obtained are marked with the symbol " [⋆] " following the measured value.

we obtain large error bars because the photometric accuracy of the data is several times lower than for UTas, and furthermore, the data taken during the source crossing are all located close to the limb, in the region of less sensitivity to limb darkening. We note that the LLDC we obtain is higher than UTas's, which is

expected, because Auckland's clear filter is known to peak between red and infrared and LLDCs usually decrease towards the infrared.

Starting from these models, we include different combinations of other data sets. If we base our analysis on the LLDC
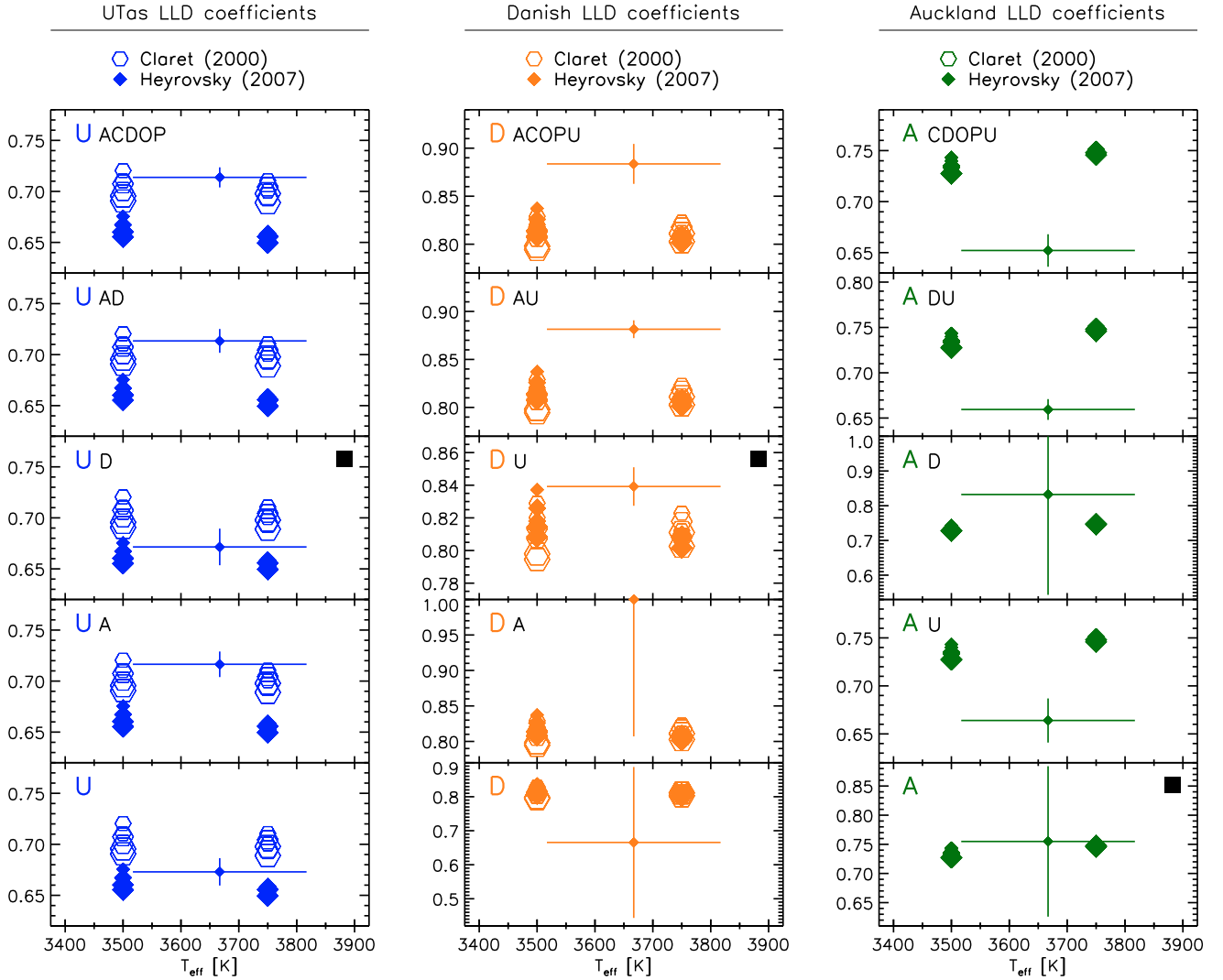
Fig. 4. Graphical representation of the linear limb-darkening measurements (crosses) for the three data sets with sensitivity to limb-darkening: UTas in the *I*-band, Danish in the *R*-band, and Auckland in a clear filter. The open hexagons and the filled diamonds are the predictions from Claret (2000) and Heyrovský (2007) linear limb-darkening (LLD) coefficients. The fitting of the light curve is performed for different combinations of telescopes (same letter conventions as for Table 2), and the results are discussed in Sect. 5. The adopted measurements are those marked with black squares in the upper right of the panels.

measurement from our best data set, UTas, then we find two distinct behaviours: either the UTas's LLDC is not displaced from the individual fit ($a \simeq 0.67$, e.g. U or U+D) or is slightly modified ($a \simeq 0.71$, e.g. U+A or all telescopes). Interestingly, when combining U and D data, the fit is stabilised for D. This is because the common fitting parameters (u_0, t_0, t_E, ρ_*) are better constrained. However, combining A with U data modifies the LLDCs compared to A and U modelled alone. This is also true when combining U+D+A or all telescopes. That Auckland modifies UTas's LLD (our best-suited data set for LLDC measurements) when the two data sets are combined, lead one to be careful about the interpretation of Auckland's LLD (besides the large error bar on the LLDC).

From this, we conclude that a precise measuring of LLDC requires a very careful study: first, one has to identify the data sets that can potentially provide a limb-darkening measurement with enough sensitivity, based on the light-curve sampling as discussed in Sect. 3.3. Then, one has to check whether the inclusion of additional data sets affects the results. Indeed, as we

have shown for this microlensing event, adding more data sets to the light curve modelling can lead to two opposite effects: either the new data stabilise the fit and help obtain LLDCs for more data sets, or they perturb the LLDC measurements. The latter may happen if unknown systematic effects are affecting the data. For OGLE 2004-BLG-482, the most reliable LLDCs for UTas and Danish are obtained when these data sets are combined in the fit (U+D). No definitive conclusion can be safely drawn for Auckland LLD, although its best estimation is likely to be obtained using A data alone. The relevant measurements we discuss below are marked in Fig. 4 with a black square in the upper right of the corresponding panels. When the fit is performed using the formula of Heyrovský (2003), we obtain similar results for the combinations U+D and A: $a_U = 0.655^{+0.010}_{-0.016}$, $a_D = 0.825^{+0.023}_{-0.022}$ and $a_A = 0.751^{+0.083}_{-0.096}$.

In order to compare our measurements to linear limb-darkening predictions from atmosphere models, we use two sets of LLDCs computed from Kurucz's ATLAS models, for which

hydrostatic equilibrium and LTE were assumed (e.g. Kurucz 1992, 1994). The first set of LLDCs is taken from Claret (2000), using the VizieR database, for the whole available range of temperatures and $\log g$ compatible with OGLE 2004-BLG-482's source star fundamental parameters (Sect. 4); we assume a solar metallicity to be consistent with our spectral analysis. The corresponding LLDCs are plotted in Fig. 4 as thin, open hexagons. We find twelve models that correspond to our requirements: two different temperatures (3500 and 3750 K), three $\log g$ (1.0, 1.5 and 2.0, plotted from smaller to bigger symbols) and for each configuration two microturbulent velocities (1 and 2 km s^{-1}). The second set of LLDCs is plotted as filled diamonds, and correspond to coefficients computed using the interpolation method advocated by Heyrovský (2007). These are computed for the same stellar parameters as before.

Evidently our LLDC measurements agree very well with the predictions from atmosphere models. For UTas I, our measurement is compatible with both the predictions from Claret (2000) and Heyrovský (2007). For the Danish R filter, the agreement is also very good, although our measurement is slightly larger than the prediction. For the Auckland clear filter, only Heyrovský (2007) predictions are available; but within the large error bars commented on previously, the data are fairly compatible with the predictions.

6. PCA-based limb-darkening coefficients

Although stellar limb darkening is usually modelled by analytical laws, another option is to construct new bases of functions directly from model-atmosphere limb-darkening profiles. In this section, we use a limb-darkening basis numerically constructed by principal component analysis (PCA and PCA LD in the following) for a set of given model atmosphere limb-darkening profiles, following Heyrovský (2003).

In this approach, the stellar intensity profile is expressed as

$$I(r) = \sum_i \alpha_i f_i(r), \qquad (6)$$

in place of Eq. (1), where the $f_i(r)$ are the PCA basis functions and α_i the corresponding coefficients. For our analysis we used a very general PCA basis constructed from the *BVRI* profiles of the full Kurucz (1992) ATLAS model-atmosphere grid (see Heyrovský 2008 for details). The resulting three first basis functions, computed for a set of atmosphere models that match the stellar parameters of OGLE 2004-BLG-482's source star, are displayed in Fig. 5.

In the simplest case of a 2-term PCA LD law (the analogue of the analytical linear limb-darkening law, LLD), the relevant parameter that defines the shape of the star's brightness profile is $\kappa \equiv \alpha_2/\alpha_1$. With our choice of PCA basis, all possible profiles are obtained by varying κ in the range $[-0.162, 0.090]$, from the most peaked to the flattest limb-darkening profiles.

We performed the OGLE 2004-BLG-482 analysis using the Heyrovský (2003) formalism for different combinations of data sets in a similar way as in Sect. 5. The results are presented in Fig. 6 for the combinations of data sets that were selected in the previous section (Fig. 4 panels with a black square in the upper right).

As for the classical LLD law discussed in detail in the previous section, we find a very good agreement between model predictions and our measurements. This shows that PCA LD provides an interesting alternative to analytical models of stellar brightness profiles. For applications where LD is not fitted (e.g., Kubas et al. 2008), it can be interesting to use PCA rather
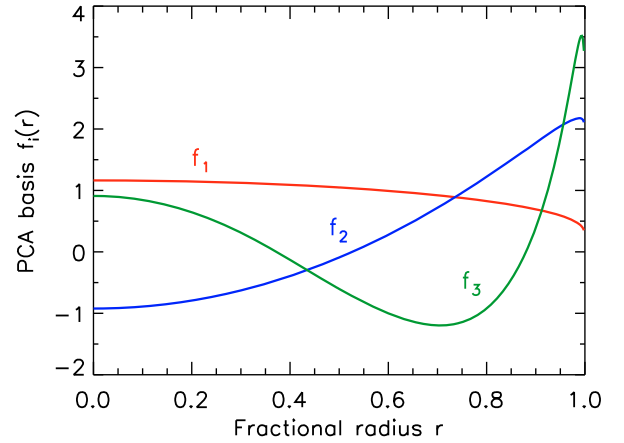
Fig. 5. First three basis functions of the PCA decomposition, computed for a set of atmosphere models that match the stellar parameters of OGLE 2004-BLG-482's source star.

than LLD laws. On the other hand, the PCA LD law always depends on the set of selected model atmospheres. This could lead to discrepancies for instance if the parameter grid is too narrow. In addition, any PCA LD law reflects the physics included in the construction of the particular atmosphere model (e.g., variants of ATLAS, MARCS, or PHOENIX models), which may not be ideally suited for the studied star. In either of these cases, however, if the observational data are good enough, one may use the situation to one's own benefit. By trying different PCA LD laws and checking the quality of the fits and patterns in the residuals one can discriminate between different "candidate" model atmospheres. To summarize, in limb-darkening modelling LLD has the advantage of simplicity and analyticity, while PCA LD has the advantage of providing better accuracy and flexibility.

7. Conclusion

We have analysed OGLE 2004-BLG-482, a relatively high-magnification single-lens microlensing event with notable extended-source effects, which was densely covered by our telescope networks. We derived precise limb-darkening measurements of the source star, a cool M giant, in particular in the I and R bands by combining the UTas and Danish data sets. No definitive conclusion could be made for Auckland data, affected by unknown systematics that prevented the data to be well-fitted along with other data; however, when the Auckland data are fitted alone, the derived limb-darkening agrees to model predictions, but with a large uncertainty.

It provided us with the rather rare opportunity to directly test model-atmosphere limb-darkening predictions for the source star. This comparison was made possible because we could obtain high-resolution UVES spectra at VLT at a critical time thanks to the short activation of a ToO programme at VLT, from which we could precisely estimate the star's fundamental parameters. The source typing has been confirmed with good precision by our photometric diagnostic based on a calibrated colour−magnitude diagram of the field. We have performed a very detailed modelling to evaluate the impact of including data sets in the modelling process, and provide new diagnostics for future work.

Very interestingly, the measured limb darkening agrees very well with model-atmosphere predictions, both when considering
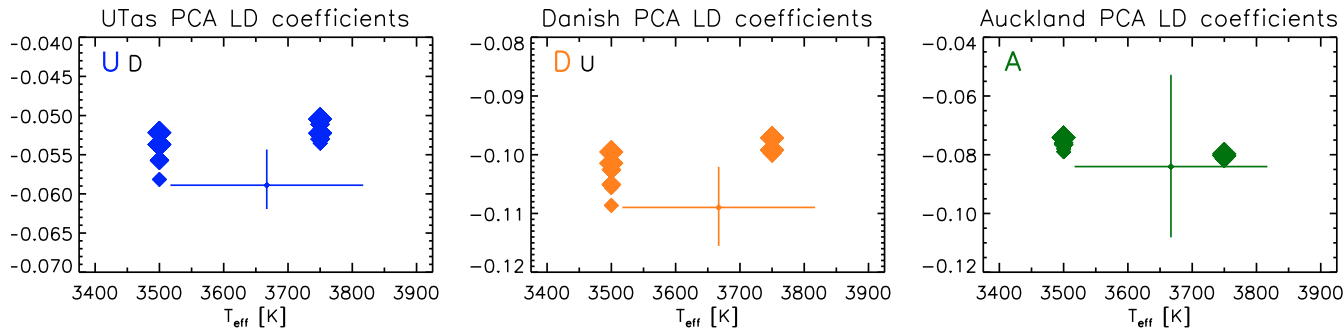
Fig. 6. PCA limb-darkening (PCA LD) coefficients κ measured (crosses) and predicted (diamonds, Heyrovský 2008) using the 2-term PCA LD as explained in the text. Letters and colours have the same meaning as in Fig. 4.

linear limb-darkening profiles, or an alternative limb-darkening description based on a principal component analysis of ATLAS stellar atmosphere models. From this study, where the precision has been pushed to a high level, we conclude that this late M giant does not suffer from any clear discrepancy between limb-darkening model predictions and measurements, which has been pointed out for earlier K giants. Although it is based on the observation of a single event, it is very likely that the conclusion can be extended to similar late M giants.

References

Abe, F., Bennett, D. P., Bond, I. A., et al. 2003, A&A, 411, L493
Afonso, C., Alard, C., Albert, J. N., et al. 2000, ApJ, 532, 340
Afonso, C., Albert, J. N., Andersen, J., et al. 2001, A&A, 378, 1014
Alard, C., & Lupton, R. H. 1998, ApJ, 503, 325
Albrow, M. D., Beaulieu, J.-P., Caldwell, J. A. R., et al. 1999a, ApJ, 522, 1022
Albrow, M. D., Beaulieu, J.-P., Caldwell, J. A. R., et al. 1999b, ApJ, 512, 672
Albrow, M. D., Beaulieu, J.-P., Caldwell, J. A. R., et al. 1999c, ApJ, 522, 1011
Albrow, M. D., Beaulieu, J.-P., Caldwell, J. A. R., et al. 2000, ApJ, 534, 894
Albrow, M. D., Horne, K., Bramich, D. M., et al. 2009, MNRAS, 397, 2099
Albrow, M. D., An, J., Beaulieu, J.-P., et al. 2001, ApJ, 549, 759
Alcock, C., Allen, W. H., Allsman, R. A., et al. 1997, ApJ, 491, 436
Bessell, M. S., & Brett, J. M. 1988, PASP, 100, 1134
Bessell, M. S., Castelli, F., & Plez, B. 1998, A&A, 333, 231
Bonatto, C., Bica, E., & Girardi, L. 2004, A&A, 415, 571
Bramich, D. M. 2008, MNRAS, 386, L77
Cassan, A., Beaulieu, J. P., Brillant, S., et al. 2004, A&A, 419, L1
Cassan, A., Beaulieu, J.-P., Fouqué, P., et al. 2006, A&A, 460, 277
Cassan, A., Horne, K., Kains, N., Tsapras, Y., & Browne, P. 2010, A&A, 515, A52
Castro, S., Pogge, R. W., Rich, R. M., DePoy, D. L., & Gould, A. 2001, ApJ, 548, L197
Claret, A. 2000, A&A, 363, 1081
Dominik, M. 2004, MNRAS, 352, 1315
Einstein, A. 1936, Science, 84, 506
Fields, D. L., Albrow, M. D., An, J., et al. 2003, ApJ, 596, 1305
Gaudi, B. S., & Gould, A. 1999, ApJ, 513, 619
Gillessen, S., Eisenhauer, F., Trippe, S., et al. 2009, ApJ, 692, 1075

Gradshteyn, I. S., & Ryzhik, I. M. 1965, Table of integrals, series and products
Groenewegen, M. A. T. 2004, MNRAS, 353, 903
Groenewegen, M. A. T. 2008, A&A, 488, 935
Gustafsson, B., Bell, R. A., Eriksson, K., & Nordlund, A. 1975, A&A, 42, 407
Gustafsson, B., Edvardsson, B., Eriksson, K., et al. 2003, in Stellar Atmosphere Modeling, ed. I. Hubeny, D. Mihalas, & K. Werner, ASP Conf. Ser., 288, 331
Gustafsson, B., Edvardsson, B., Eriksson, K., et al. 2008, A&A, 486, 951
Hendry, M. A., Coleman, I. J., Gray, N., Newsam, A. M., & Simmons, J. F. L. 1998, New Astron. Rev., 42, 125
Heyrovský, D. 2003, ApJ, 594, 464
Heyrovský, D. 2007, ApJ, 656, 483
Heyrovský, D. 2008, in PoS: Manchester microlensing conference, ed. E. Kerins, S. Mao, N. Rattenbury, & L. Wyrzykowski, 28
Heyrovský, D., Sasselov, D., & Loeb, A. 2000, ApJ, 543, 406
Houdashelt, M. L., Bell, R. A., Sweigart, A. V., & Wing, R. F. 2000, AJ, 119, 1424
Jiang, G., DePoy, D. L., Gal-Yam, A., et al. 2004, ApJ, 617, 1307
Kains, N., Cassan, A., Horne, K., et al. 2009, MNRAS, 395, 787
Kubas, D., Cassan, A., Beaulieu, J. P., et al. 2005, A&A, 435, 941
Kubas, D., Cassan, A., Dominik, M., et al. 2008, A&A, 483, 317
Kupka, F., Piskunov, N., Ryabchikova, T. A., Stempels, H. C., & Weiss, W. W. 1999, A&AS, 138, 119
Kurucz, R. 1994, Solar abundance model atmospheres for 0,1,2,4,8 km s^{-1}. Kurucz CD-ROM No. 19. Cambridge, Mass.: Smithsonian Astrophysical Observatory, 19
Kurucz, R. L. 1992, in The Stellar Populations of Galaxies, ed. B. Barbuy, & A. Renzini, IAU Symposium, 149, 225
Levesque, E. M., Massey, P., Olsen, K. A. G., et al. 2005, ApJ, 628, 973
Levesque, E. M., Massey, P., Olsen, K. A. G., & Plez, B. 2007, ApJ, 667, 202
Loeb, A., & Sasselov, D. 1995, ApJ, 449, L33
Massey, P., Levesque, E. M., Plez, B., & Olsen, K. A. G. 2008, e-prints, 801
Paczyński, B. 1986, ApJ, 304, 1
Paczyński, B., & Stanek, K. Z. 1998, ApJ, 494, L219
Plez, B. 1998, A&A, 337, 495
Plez, B., Brett, J. M., & Nordlund, A. 1992, A&A, 256, 551
Plez, B., van Eck, S., Jorissen, A., et al. 2003, in Modelling of Stellar Atmospheres, ed. N. Piskunov, W. W. Weiss, & D. F. Gray, IAU Symposium, 210, 2P
Rattenbury, N. J., Mao, S., Sumi, T., & Smith, M. C. 2007, MNRAS, 378, 1064
Salaris, M., & Girardi, L. 2002, MNRAS, 337, 332
Sasselov, D. D. 1996, in Cool Stars, Stellar Systems, and the Sun, ed. R. Pallavicini & A. K. Dupree, ASP Conf. Ser., 109, 541
Strassmeier, K. G., & Schordan, P. 2000, Astron. Nachr., 321, 277
Sumi, T. 2004, MNRAS, 349, 193
Thurl, C., Sackett, P. D., & Hauschildt, P. H. 2006, A&A, 455, 315
Udalski, A. 2003, Acta Astron., 53, 291
Valls-Gabaud, D. 1995, in Large Scale Structure in the Universe, ed. J. P. Mücket, S. Gottloeber, & V. Müller, 326
Witt, H. J. 1995, ApJ, 449, 42
Witt, H. J., & Mao, S. 1994, ApJ, 430, 505
Yoo, J., DePoy, D. L., Gal-Yam, A., et al. 2004, ApJ, 603, 139

[1] Astronomisches Rechen-Institut (ARI), Zentrum für Astronomie der Universität Heidelberg (ZAH), Mönchhofstr. 12–14, 69120 Heidelberg, Germany
e-mail: zub@ari.uni-heidelberg.de
[2] International Max-Planck-Research School for Astronomy & Cosmic Physics at the University of Heidelberg, Germany

3 Institute of Astronomy, University of Zielona Góra, Lubuska st. 2, 65-265 Zielona Góra, Poland

4 The PLANET Collaboration

5 Institut d'Astrophysique de Paris, UMR 7095 CNRS – Université Pierre & Marie Curie, 98bis Bd Arago, 75014 Paris, France

6 Institute of Theoretical Physics, Charles University, V Holešovičkách 2, 18000 Prague, Czech Republic

7 LATT, Université de Toulouse, CNRS, 31400 Toulouse, France

8 Department of Physics and Astronomy, Box 516, 751 20 Uppsala, Sweden

9 University of Canterbury, Department of Physics & Astronomy, Private Bag 4800, Christchurch, New Zealand

10 European Southern Observatory (ESO), Casilla 19001, Vitacura 19, Santiago, Chile

11 Auckland Observatory, PO Box 24-197, Auckland, New Zealand

12 The μFUN Collaboration

13 University of St Andrews, School of Physics & Astronomy, North Haugh, St Andrews, KY16 9SS, UK

14 Department of Astronomy, Ohio State University, 140 W. 18th Ave., Columbus, OH 43210, USA

15 University of Notre Dame, Physics Department, 225 Nieuwland Science Hall, Notre Dame, IN 46530, USA

16 Institute of Geophysics and Planetary Physics, L-413, Lawrence Livermore National Laboratory, PO Box 808, Livermore, CA 94550, USA

17 Department of Physics, University of Rijeka, Omladinska 14, 51000 Rijeka, Croatia

18 Technical University of Vienna, Dept. of Computing, Wiedner Hauptstrasse 10, Vienna, Austria

19 University of Tasmania, Physics Department, GPO 252C, Hobart, Tasmania 7001, Australia

20 Niels Bohr Institute and Centre for Star and Planet Formation, Juliane Mariesvej 30, 2100 Copenhagen, Denmark

21 NASA Exoplanet Science Institute, Caltech, MS 100-22, 770 South Wilson Avenue Pasadena, CA 91125, USA

22 Perth Observatory, Walnut Road, Bickley, Perth 6076, Australia

23 South African Astronomical Observatory, PO Box 9 Observatory 7935, South Africa

24 Space Telescope Science Institute, 3700 San Martin Drive, Baltimore, MD 21218, USA

25 Astrophysics Group, Faculty of Physics, Weizmann Institute of Science, Rehovot 76100, Israel

26 Department of Physics, Institute for Basic Science Research, Chungbuk National University, Chongju 361-763, Korea

27 School of Physics and Astronomy and the Wise Observatory, Raymond and Beverly Sackler Faculty of Exact Sciences, Tel-Aviv University, Tel Aviv 69978, Israel

28 School of Physics and Astronomy, Tel-Aviv University, Tel-Aviv 69978, Israel

29 Division of Physics, Mathematics and Astronomy, California Institute of Technology, Pasadena, CA

30 Korea Astronomy and Space Science Institute, Daejon 305-348, Korea

31 Farm Cove Observatory, Centre for Backyard Astrophysics, Pakuranga, Auckland New Zealand

32 Warsaw University Observatory. Al. Ujazdowskie 4, 00-478 Warszawa, Poland

33 Universidad de Concepción, Departamento de Física, Casilla 160-C, Concepción, Chile

34 Institute of Astronomy, University of Cambridge, Madingley Road, CB3 0HA Cambridge, UK